Plasma Sources
Science and
Technology

PURPOSE-LED
PUBLISHING™

PAPER • **OPEN ACCESS**

Spatial profile of argon ($1s_5$) metastables in an electron beam generated plasma

To cite this article: V S Santosh K Kondeti *et al* 2025 *Plasma Sources Sci. Technol.* **34** 115012

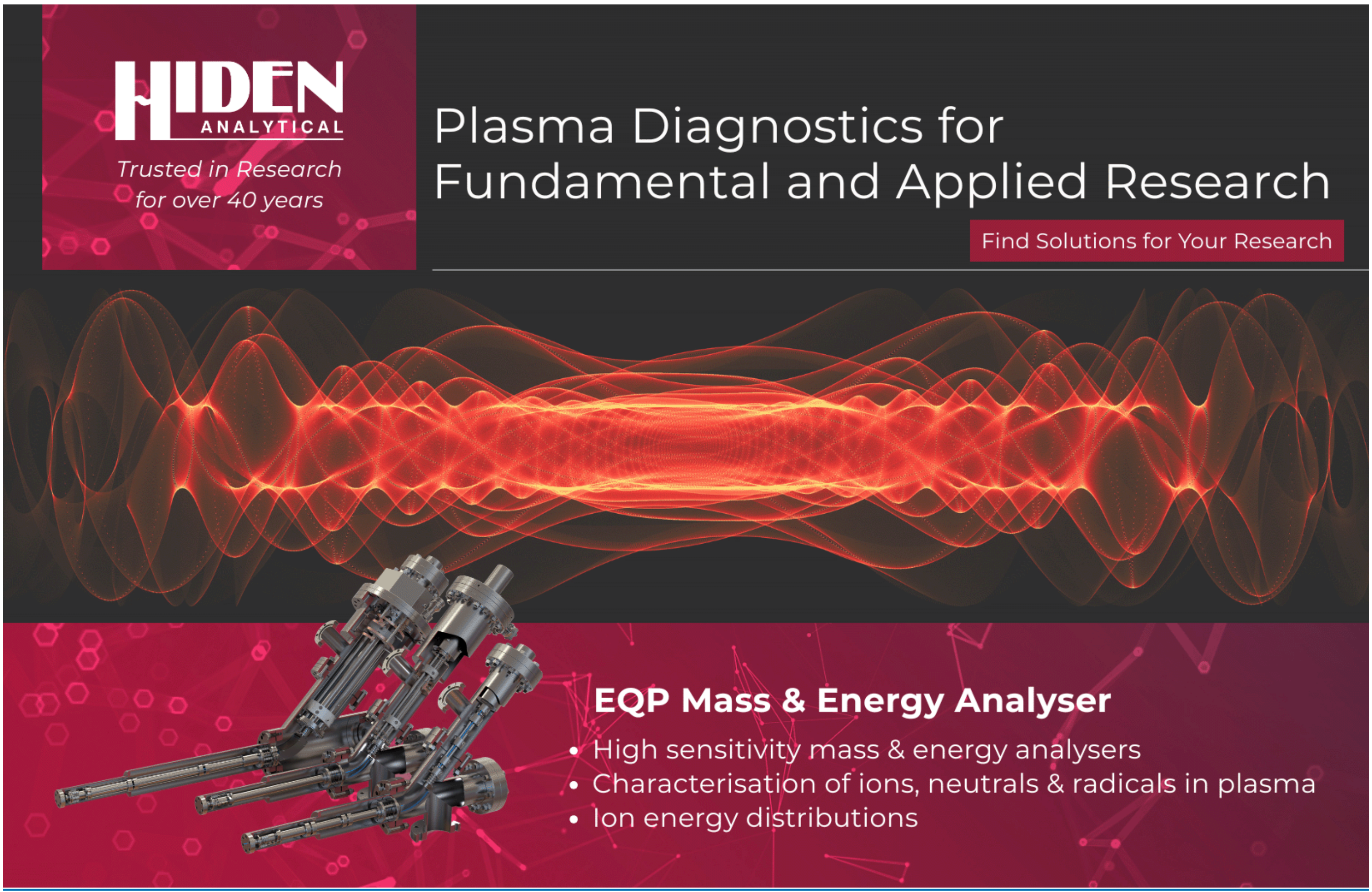

OPEN ACCESS
IOP Publishing
Plasma Sources Science and Technology
Plasma Sources Sci. Technol. **34** (2025) 115012 (8pp)
https://doi.org/10.1088/1361-6595/ae186f

Spatial profile of argon ($1s_5$) metastables in an electron beam generated plasma

V S Santosh K Kondeti*, Nirbhav S Chopra, Shurik Yatom and Yevgeny Raitses

Princeton Plasma Physics Laboratory, Princeton, NJ 08540, United States of America

E-mail: vkondeti@pppl.gov

Received 22 May 2025, revised 16 September 2025
Accepted for publication 28 October 2025
Published 24 November 2025

Abstract

Electron beams with an applied magnetic field generate a secondary cold plasma with a selective chemical composition, featuring low-energy ions and metastable species in the discharge periphery, ideal for low-damage plasma treatment of material substrates. In this work, we studied the plasma generated by an e-beam using a 4 kV voltage in a pure argon gas environment under a magnetic field of 150 G and in the pressure range of 25–90 mTorr. We measured the absolute spatial density profile of argon ($1\ s_5$) metastables in an electron beam generated plasma by laser-induced fluorescence and found it to be of the order of $10^{16}\ m^{-3}$. The electron temperature and the electron density measured by a Langmuir probe were of the order of $10^{16}\ m^{-3}$ and less than an eV respectively. Electron-impact quenching was identified as a significant loss mechanism for the $Ar(1s_5)$ state, leading to the saturation of the metastable density at higher pressures. Outside the primary ionization region, the spatial distribution of argon metastables followed a linear diffusion profile, indicating negligible additional production in those regions.

Keywords: electron beam, argon metastables, laser-induced fluorescence, spatial profile, EEDF

1. Introduction

The semiconductor fabrication of microelectronics chips in the present era requires sub-nm precision accuracy to enable technologies such as 3 nm and 2 nm nodes [1]. Processes such as atomic layer etching, atomic layer deposition, and area selective deposition are often used to achieve such precision [2–4]. Even ions with an energy greater than a few electron volts (eV) can alter the surface of the material [5]. Achieving high precision without damage to the material surface will require meticulous control over the ion energy and the chemical composition near the material surface.

Plasma-produced argon metastables have a large energy of over 11.5 eV. Being a non-resonant state, the argon metastable levels typically possess orders of magnitude longer lifetime, up to several seconds, compared to the other reactive species in the plasma such as electrons, radicals and ions [6, 7]. Hence, they have the potential to deliver reactivity at distances away from the region where they are generated. In an argon-silane radio frequency plasma, Sansonnens *et al* suggested that argon metastables were quenched by silane molecules resulting in an increased dissociation rate of silane [8]. Sukhinin *et al* modeled an electron beam plasma without a magnetic field in an argon-silane gas mixture [7]. They demonstrated

---

[*] Author to whom any correspondence should be addressed.

that the dissociation efficiency of silane by metastable argon atoms can be comparable to the dissociation achieved through the direct electron-impact collision of silane with the electron beam. However, beyond the beam region, the density of the argon metastables was shown to drop sharply due to quenching collisions with monosilane molecules.

Electron beam (e-beam) generated plasmas in an applied magnetic field have great potential for their use in the processing of materials by enabling control over the electron energy [9, 10]. The ionization is driven by a magnetically confined e-beam plasma with energies in the range of 1–10 keV. The beam electrons interact with the background gas and generate a secondary plasma with a low electron temperature that is typically less than 1 eV, a high electron density, and ion energies of a few eV. They are capable of delivering a large flux of reactive species to an adjacent material surface without material damage [11, 12]. Argon metastables can be carriers of energy and can produce reactive chemistry outside the active electron beam region. Although the energy of the beam electrons is too large to contribute significantly to metastable production, the secondary electrons in the discharge can produce the metastable states [13]. The significant production of argon metastables achieved by the e-beam generated plasma is attractive for remote low-temperature and damage-free processing of materials away from the energetic e-beam. While magnetically confined e-beam plasmas have been characterized with respect to electron properties and ion energies, studies of metastable species production have been limited and have been mostly confined to simulation models [13–17]. Yatom *et al* experimentally studied the effect of N_2 admixture to argon in an e-beam generated plasma [13]. They reported a reduction in the Ar($1s_5$) density with increasing concentrations of N_2 both in the e-beam region and the periphery of the discharge. This reduction was attributed to the excitation exchange with nitrogen molecules and the cooling of plasma electrons through inelastic collisions with these molecules.

In this work, we used laser-induced fluorescence to analyze the spatial absolute density profile of the Ar($1s_5$) metastable level generated by a magnetic field confined e-beam plasma operated in an argon gas environment. The absolute density of the Ar($1s_5$) metastable level was obtained by a five-level population kinetics model and calibrated using Rayleigh scattering in air. These measurements were coupled with measurements of the electron temperature and the electron density using a Langmuir probe. We show that the Ar($1s_5$) metastables are formed in the e-beam region and diffuse towards the periphery. We identify the dominant loss pathway for the quenching of the Ar($1s_5$) level.

2. Methods

2.1. Plasma setup

The plasma source consists of an e-beam generated plasma in an applied magnetic field, the same as the one used in our previous work [13]. The plasma source was built with a similar design as the one designed by the Naval Research Laboratory, but with a cylindrical geometry [18, 19]. A 2.75 inch conflat (CF) flange is attached concentrically to the horizontal end of a six-way cross vacuum chamber. The dimensions of the chamber and the electrical parameters used to generate the plasma have been tabulated in table 1. A voltage of −4 kV is applied to the CF flange by a DC power supply (Glassman ER series), which acts as a cathode. The CF flange is electrically isolated from the vacuum chamber by a ceramic disk and rubber gaskets. A mechanical pump was used to evacuate the chamber to a base pressure of less than 2 mTorr. A leak valve was used to fill the chamber with argon gas to a pressure between 25 and 90 mTorr. The e-beam was confined by a magnetic field of 150 G applied along the direction of the propagation of the e-beam and directed away from the cathode by a pair of coils in Helmholtz configuration. The coils were water-cooled and powered by a DC power supply (Kepko, KLN 20–76). The e-beam terminates on a glass viewport. This termination is different from the plasma source reported by NRL where all electrons were collected by a beam dump [9]. In our configuration, a majority of the electrons are confined in the axial direction between the cathode and the floating dielectric wall. Only energetic electrons capable of overcoming the floating sheath potential at the dielectric wall are lost to the wall. Note that the e-beam induced secondary electrons may originate from this dielectric wall. However, their role in the formation of plasma and metastables is beyond the scope of this manuscript. The discharge current was monitored on the DC power supply. A schematic of the experimental setup is shown in figure 1. The vacuum chamber was equipped with glass viewports for optical diagnostics.

Table 1. Properties of the e-beam device used in this work.

Property	Parameter
Pressure	25–90 mTorr
Cathode voltage	−4 kV
Discharge current	1.6–5.5 mA
Chamber diameter	20 cm
Chamber length	40 cm
Magnetic field	150 G

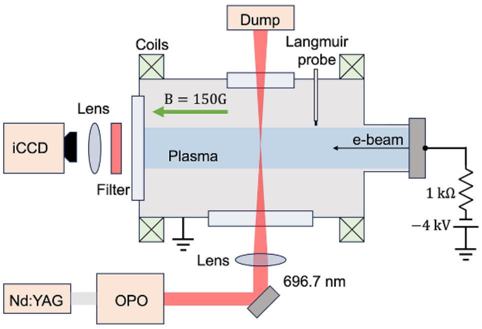

Figure 1. Schematic of the electron beam generated plasma source together with the laser-induced fluorescence diagnostic setup.

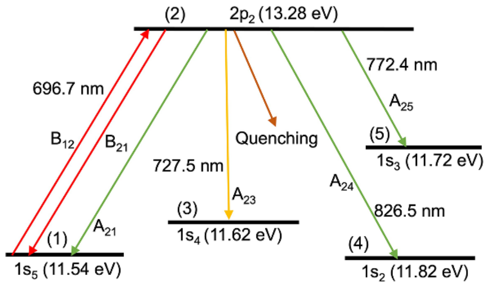

Figure 2. Transition scheme for a five-level population kinetics model. B$_{ij}$: Einstein absorption coefficient from level i to j and A$_{ij}$: Einstein emission coefficient from level i to j.

2.2. Laser induced fluorescence (LIF)

LIF diagnostic was used to obtain the absolute density of the Ar(1s$_5$) metastable level. A detailed description of the diagnostic method, the five-level population kinetics model (figure 2) and the calibration by Rayleigh scattering to obtain the absolute density of Ar(1s$_5$) metastable level has been provided in [13]. Briefly, an optical parametric oscillator (OPO) laser (Horizon) pumped by an Nd:YAG laser (Amplitude-Continuum) is set to the transition wavelength of 696.7 nm to excite the Ar(1s$_5$) level to the Ar(2p$_2$) level. The laser beam is focused radially on to center of the e-beam by using a plano-convex lens with a focal length of 100 cm. The laser energy was adjusted to 4.6 μJ using a neutral density filter to be in the linear LIF regime [20]. Fluorescence was observed during de-excitation to the Ar(1s$_4$) level. An optical filter (Thorlabs FL730-10, centered at 730 nm with a full width at half maximum of 10 nm) was installed in front of an iCCD camera (Princeton Instruments, PIMax 3) to collect fluorescence at a wavelength of 727.5 nm in a direction perpendicular to the direction of the laser beam propagation. The camera gate was set to 50 ns to collect all the fluorescence signal for a period of 50 ns after the laser beam resulting from the de-excitation of the Ar(2p$_2$) level to the Ar(1s$_4$) level. In the investigated pressure range of 25–90 mTorr, the correction for quenching of the Ar(2p$_2$) to deduce the Ar(1s$_5$) density can be ignored as quenching is negligible compared to the radiative relaxation from the Ar(2p$_2$) level [13]. The schematic of the laser-induced fluorescence diagnostic setup is shown in figure 1. A delay generator (Berkeley Nucleonics, BNC 575) was used to synchronize the laser beam with the iCCD camera. Rayleigh scattering of air was used to calibrate the fluorescence intensity and a five-level model was used to calculate the absolute density of the Ar(1s$_5$) level. A schematic of five-levels considered in the model together with their energies is shown in figure 2.

2.3. Langmuir probe measurements

A Langmuir probe was used to measure the electron density and the electron temperature of the secondary electrons produced by the e-beam. The probe was made out of a tungsten wire with a diameter of 0.1 mm and a length of 3.3 mm. The probe was insulated by ceramic and molybdenum tubes installed concentrically around the probe. A reference probe with a diameter of 1.3 mm and a length of 4.5 mm was positioned above the concentric probe construction to create a reference to eliminate distortions in the floating potential measurements during the measurement of the probe voltage-current characteristics. The location of the Langmuir probe measurements was 7 cm away from the LIF measurements along the e-beam path (figure 1). Walton *et al* measured the plasma density profile along the propagation direction of a similar e-beam plasma and found only minor variations along the beam path [9]. For the experimental conditions considered in this work, the radius of the Langmuir probe was smaller than the electron Larmor radius, the electron-neutral collisional mean free path and the electron Debye length. The probe sheath was estimated by assuming it to be non-magnetized and collisionless. The electron energy distribution function (EEDF) was determined from the second derivative of the electron current with respect to the probe voltage (Druyvesteyn method) [21–23]. A detailed explanation of the Langmuir probe setup has been described in [13]. The effects of secondary electron emission due to the beam electrons are negligible for our regime [24, 25].

2.4. Ar(1s$_5$) production and loss processes

The Ar(1s$_5$) metastables in pure argon atmosphere are produced predominantly by the radiation from the Ar(2p) levels, the direct excitation from the ground state and the collisional de-excitation from the Ar(1s$_4$) level, while they are lost via electronic quenching to the ground state, excitation to the Ar(1s$_4$), the Ar(2s$_1$) and the Ar(2p) levels [13, 26]. Among the production pathways, the radiation from the Ar(2p) levels and direct excitation from the ground state are the dominant pathways [13, 15].

The reaction rate coefficients of the different Ar levels produced by the plasma electrons used in the estimation of the Ar(1s$_5$) production rate have been tabulated in table 2. The electron-impact cross-sections for e-beam excitation have been tabulated in table 3, while the radiative transition probabilities from all the different Ar(2p$_{1-10}$) levels to the Ar(1s$_5$) level have been summarized in table 4. The Ar(2p) level used in tables 2–5 is the Ar(2p) lumped state including 2p$_{2-10}$ levels other than the Ar(2p$_6$) and the Ar(2p$_9$) levels.

The beam current density (J_b) can be determined from the current measured by the power supply (I) and the cross-sectional area of the beam,

$$J_\mathrm{b} = \frac{I}{\pi r_\mathrm{b}^2} \tag{1}$$

where r_b is the effective radius of the beam. The e-beam broadens with an increase in pressure due to scattering and r_b increases with pressure [26]. Hence, r_b as a function of pressure can be estimated as the width of the ionization region discussed in section 3.3. The production rate by the beam (R_b)

Table 2. Reaction rate coefficients of the production processes of Ar(1s$_5$) level assuming a Maxwellian EEDF [26]. T_e is the electron temperature in the units of eV.

Sl No.	Reaction	Reaction rate coefficient, k (cm^{3}s$^-$1)	References
P$_1$	Ar + e → Ar(1s$_5$) + e	$k_{P_1} = 1.0\times10^{-8}T_e^{-0.5}\mathrm{e}^{-13.5/T_e}$	[26, 27]
P$_2$	Ar + e → Ar(2p$_9$) + e	$k_{P_2} = 4.5\times10^{-9}T_e^{-0.4}\mathrm{e}^{-14.5/T_e}$	[26, 27]
P$_3$	Ar + e → Ar(2p$_6$) + e	$k_{P_3} = 1.5\times10^{-9}T_e^{-0.3}\mathrm{e}^{-14/T_e}$	[26, 27]
P$_4$	Ar + e → Ar(2p) + e	$k_{P_4} = 1.8\times10^{-8}T_e^{-0.4}\mathrm{e}^{-14.5/T_e}$	[26, 27]

Table 3. Cross-section of the production processes of Ar(1s$_5$) level by the electron beam [26]. E$_b$ is the electron beam energy in the units of keV.

Sl No.	Reaction	Cross-section, σ (cm^2)	References
P$_5$	Ar + e$_b$ → Ar(1s$_5$) + e$_b$	$\sigma_{P_5} = 7\times10^{-24}\ \mathrm{E}_b^{-4}$	[27]
P$_6$	Ar + e$_b$ → Ar(2p$_9$) + e$_b$	$\sigma_{P_6} = 1\times10^{-19}\ \mathrm{E}_b^{-1/2}$	[27]
P$_7$	Ar + e$_b$ → Ar(2p$_6$) + e$_b$	$\sigma_{P_7} = 3\times10^{-19}\ \mathrm{E}_b^{-2/3}$	[27]
P$_8$	Ar + e$_b$ → Ar(2p) + e$_b$	$\sigma_{P_8} = 2\times10^{-18}\ \mathrm{E}_b^{-1/2}$	[27]

Table 4. The transition probability of the radiative processes used in the estimation of the production of the Ar(1s$_5$) level.

Transition	Transition probability, A (s^{-1})	References
Ar(2p$_9$) → Ar(1s$_5$) + hν	$A_1 = 3.30\times\ 10^7$	[28, 29]
Ar(2p$_6$) → Ar(1s$_5$) + hν	$A_2 = 2.45\times10^7$	[28, 29]
Ar(2p$_6$) → Ar(1s$_4$) + hν	$A_3 = 0.49\times10^7$	[28, 29]
Ar(2p$_6$) → Ar(1s$_2$) + hν	$A_4 = 0.50\times10^7$	[28, 29]
Ar(2p) → Ar(1s$_2$) + hν	$A_5 = 5.27\times10^7$	[28, 29]
Ar(2p) → Ar(1s$_3$) + hν	$A_6 = 3.37\times10^7$	[28, 29]
Ar(2p) → Ar(1s$_4$) + hν	$A_7 = 8.10\times10^7$	[28, 29]
Ar(2p) → Ar(1s$_5$) + hν	$A_8 = 6.86\times10^7$	[28, 29]

Table 5. Reaction rate coefficients of the loss processes of Ar(1s$_5$) level [26]. T_e is the electron temperature in the units of eV.

Sl No.	Reaction	Reaction rate coefficient, k (cm^{3}s$^-$1)	References
L$_1$	Ar(1s$_5$) + e → Ar(1s$_4$) + e	$k_{L_1} = 1.1\times10^{-7}T_e^{-0.5}$	[30]
L$_2$	Ar(1s$_5$) + e → Ar(2p$_9$) + e	$k_{L_2} = 3.14\times10^{-7}T_e^{0.208}\mathrm{e}^{-1.61/T_e}$	[31]
L$_3$	Ar(1s$_5$) + e → Ar(2p$_6$) + e	$k_{L_3} = 1.28\times10^{-7}T_e^{0.17}\mathrm{e}^{-1.7/T_e}$	[31]
L$_4$	Ar(1s$_5$) + e → Ar(2p) + e	$k_{L_4} = 2.65\times10^{-7}T_e^{0.128}\mathrm{e}^{-1.56/T_e}$	[31]
L$_5$	Ar(1s$_5$) + e → Ar(2 s$_1$) + e	$k_{L_5} = 2.53\times10^{-9}T_e^{-0.686}\mathrm{e}^{-2.13/T_e}$	[31]
L$_6$	Ar(1s$_5$) + e → Ar + e	$k_{L_6} = 2.0\times10^{-8}T_e^{-0.5}\mathrm{e}^{-1.952/T_e}$	[27]

can be calculated as follows:

$$R^b_{1s_5} = n_{\mathrm{Ar}}\frac{J_{\mathrm{b}}}{e}\sigma \tag{2}$$

where n_{Ar} is the density of argon gas, calculated using the ideal gas law by assuming a gas temperature of 400 K, e is the elementary charge and σ is the reaction cross-section (table 3). For plasma electrons, the reaction rate was calculated as the product of the reaction rate coefficient (k), n_{Ar} and the electron density (n_{e}),

$$R^p_{1s_5} = kn_{\mathrm{Ar}}n_{\mathrm{e}}. \tag{3}$$

The reaction rates of the radiative processes from the Ar(2p) levels to the Ar(1s$_5$) level were calculated by multiplying the reaction rate from equation (3) with the branching ratio for the particular transition ($R_{\mathrm{radiative}} = kn_{\mathrm{Ar}}n_{\mathrm{e}}a_{1s_5\leftarrow j}$). The branching ratio, $a_{1s_5\leftarrow j}$ is the ratio of the transition probability of the transition of interest ($1s_5 \leftarrow j$) to the sum of the transition probabilities of the possible transitions from the level j,

$$a_{1s_5\leftarrow j} = \frac{A_{1s_5\leftarrow j}}{\sum_i A_{ij}}. \tag{4}$$

The reaction rate coefficients of the loss processes considered in the estimation of the Ar(1s$_5$) loss rate have been listed in table 5. The loss reaction rate was calculated as:

$$R^L_{1s_5} = kn_{\mathrm{Ar}*}n_{\mathrm{e}} \tag{5}$$

where n_{Ar^*} is the Ar(1s$_5$) density. The diffusion loss rate can be approximated as [8, 32]:

$$L_D = \frac{\partial \Gamma_{\mathrm{Ar}*}}{\partial r} \approx \frac{D_{\mathrm{Ar}^*} n_{\mathrm{Ar}^*}}{\Lambda^2} = k^D_{\mathrm{Ar}^*} n_{\mathrm{Ar}^*} \tag{6}$$

where $\frac{\partial \Gamma_{\mathrm{Ar}*}}{\partial r}$ is the flux gradient in the radial direction and Λ is the characteristic diffusion length estimated as the chamber radius. The argon metastable diffusion coefficient in this pressure regime is: $\mathrm{D}_{\mathrm{Ar}^*} = 54 P_{\mathrm{Ar}}^{-1}\ \mathrm{cm}^{-2}\ \mathrm{s}^{-1}$, where P_{Ar} is the pressure in units of Torr [7, 32]. $k^D_{\mathrm{Ar}^*}$ is the effective diffusive loss rate (s^{-1}).

3. Results and discussion

3.1. EEDF

Figure 3 shows the EEDF in the center of the discharge measured by a Langmuir probe at a pressure of 60 mTorr. The measured currents by the Langmuir probe become small for electron energies greater than 6 eV, making the signal-to-noise ratio too small to reliably measure the EEDF profile beyond an energy of 6 eV. The energy for the formation of Ar(1s$_5$) metastable level by the direct excitation from the ground state of Ar is 11.54 eV. While the Langmuir probe could not measure the properties of the electrons responsible for the formation of the Ar(1s$_5$) level, we use the measured electron density to compare the plasma density profile to the Ar(1s$_5$) density profile.

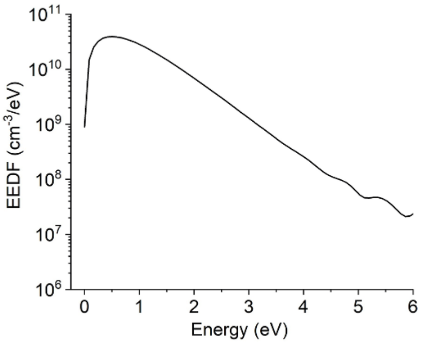

Figure 3. The electron energy distribution function (EEDF) at a pressure of 60 mTorr at the center of the discharge.

3.2. Effect of pressure

Figure 4(a) shows the variation of the current, the electron temperature and the electron density at the center of the discharge as a function of pressure. With the increase in pressure from 25 mTorr to 50 mTorr, the effective electron collision mean free path and the ionization mean free path reduce from 44 cm to 12 cm and 55 cm to 15 cm respectively [33–35]. The length of the chamber is 40 cm (table 1). With the rise in pressure, the electron-collision and the ionization mean free paths become smaller than the length scale of the device. Hence, the ionization increases with pressure due to the increase in collisions, resulting in the observed growth of the electron density (figure 4(a)). This coincides with the observed increase in the discharge current from 1.6 mA to 5.5 mA with the increase in the pressure from 25 mTorr to 90 mTorr. The discharge current is due to the radial transport of electrons and ions across the magnetic field and ion induced secondary electron emission from the quartz window. A higher plasma density leads to a greater ion flux impinging the cathode, which in turn enhances secondary electron emission and increases the discharge current. The electron density and the electron temperature were found to be of the order of $10^{16}\ \mathrm{m}^{-3}$ and less than an eV. The electron temperature increases with pressure and saturates around a pressure of 70 mTorr. The pressure dependence of the electron temperature is consistent with the simulations of Rauf *et al* [14]. Lock *et al* observed a similar increase in the electron temperature as a function of pressure for an electron beam generated plasma [10].

Figure 5 shows the production rate of the Ar(1s$_5$) level due to electron impact (both from the e-beam and plasma) and radiative transitions from all the Ar(2p) levels. The Ar(1s$_5$) level is predominantly produced by the radiation from the Ar(2p) levels. The contribution of the Ar(1s$_5$) level production rate by the plasma electrons is at least one order of magnitude lower than the radiation from Ar(2p) levels and this gap reduces with the increase in pressure for the investigated pressure regime (figure 5). The contribution from e-beam excitation is negligible, with production rates over seven orders of magnitude lower than those from the radiative transitions from the Ar(2p) levels (figure 5). Figure 5 also shows the reaction rate of the Ar(1s$_5$) loss processes and the diffusion loss determined by equation (6) as a function of pressure. The dominant loss pathway for the Ar(1s$_5$) level is the loss through collisional mixing to form the Ar(1s$_4$) state (table 5: reaction L$_1$, figure 5).

The total production rate is more than an order of magnitude lower than the total loss rate (figure 5), suggesting that there is a discrepancy in the considered parameters in the estimation of the production or the loss rates. With the rise in pressure from 25 mTorr to 90 mTorr, the electron density and the electron temperature at the center of the discharge increase by factors of about 7 and 2 respectively (figure 4(a)). However, the measured Ar(1s$_5$) density at the discharge center increases only by a factor of 1.3, saturating with the increase in pressure at 60 mTorr (figure 4(b)). The reaction rate of the total losses increase by a factor of about 10 with the rise in pressure from 25 mTorr to 90 mTorr, while the total production rate stays nearly constant in this pressure range. The pressure increases by a factor of 3.6 in this range. As a first approximation without considering the change in gas temperature, the neutral argon density increases by a factor 3.6 while the measured electron density increased by a factor 7. This would suggest an Ar(1s$_5$) density increase by a factor of about 25. However, we only observe an increase of Ar(1s$_5$) of a factor of 1.3, which is significantly lower than the first order approximation. This estimate together with the fact that the total production rate is more than an order of magnitude lower than the total

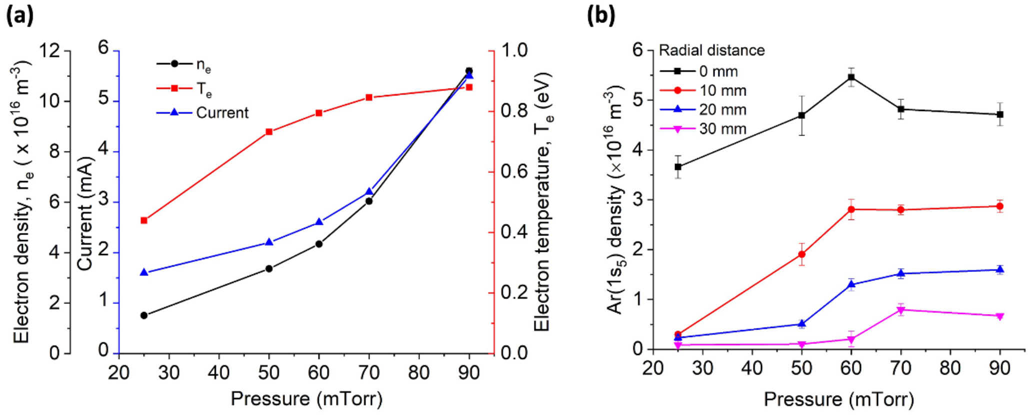

Figure 4. (a) The measured current, electron density and electron temperature at the center of the discharge as a function of pressure and (b) $Ar(1s_5)$ density as a function of pressure at different radial distances from the center of the discharge.

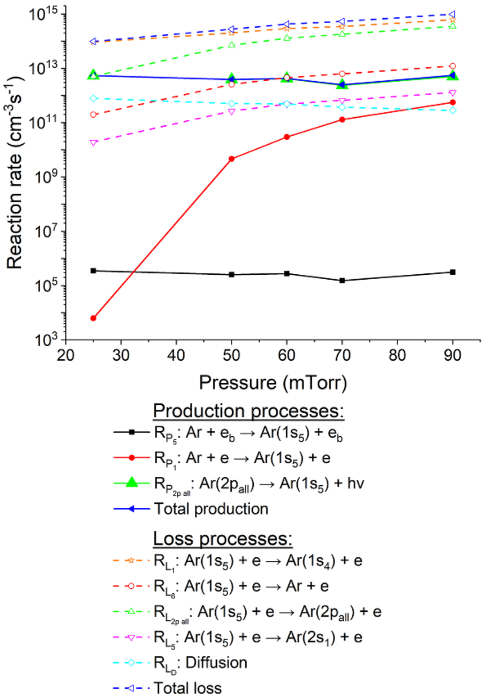

Figure 5. Reaction rates of $Ar(1s_5)$ production (solid lines) and loss processes (dashed lines) as a function of pressure. The production rates were calculated assuming a Maxwellian EEDF.

loss rate, likely suggests that the assumption of a Maxwellian EEDF is incorrect. Intermediate energy electrons with energies exceeding 11.54 eV, which are responsible for the production of the $Ar(1s_5)$ level, either through direct electronic excitation of the ground state or via radiation from the Ar(2p) levels, do not exhibit the same pressure-dependent density profile as the low-energy electrons measured by the Langmuir probe [36]. The production of the $Ar(2p_{1-10})$ levels, who radiation to the $Ar(1s_5)$ level is the dominant pathway for the production of the $Ar(1s_5)$ level, requires electrons with energy greater than 13 eV. Further, with the increase in pressure the losses due to collisions of the $Ar(1s_5)$ level with electrons likely dominates over its production processes and results in the observed saturation of $Ar(1s_5)$ density with pressure.

The $Ar(1s_5)$ density at other radial distances of 10 mm, 20 mm, and 30 mm from the center of the e-beam also increases with pressure from 25 to 60 mTorr, while it remains constant with further increase in pressure up to 90 mTorr (figure 4(b)). The increase in pressure increases the $Ar(1s_5)$ density both at the center of the e-beam and also at different radial locations. This suggests that Ar metastables can transfer their energy to peripheral locations outside the e-beam region where substrates are typically placed for material processing.

The $Ar(1s_5)$ density remains nearly constant as a function of pressure for different radial locations in the pressure range of 60–90 mTorr. While the electron quenching reaction rate drastically increases in this pressure range, the knowledge on the behavior of the electrons with energy greater that 11.54 eV that are responsible for the production of Ar (1 s_5) level can shed light on the production processes. Unfortunately, electrons with an energy greater than 11.5 eV necessary for the generation of the $Ar(1s_5)$ level could not be detected by the Langmuir probe.

3.3. Spatial variation of the $Ar(1s_5)$ density and electron properties

Figure 6(a) shows the variation of the electron temperature, the electron density and the $Ar(1s_5)$ density as a function of the radial distance at a pressure of 60 mTorr. The electron density peaks at the center of the discharge and reduces radially. This is consistent with previous experiments and simulations from a similar e-beam generated plasma [10, 14, 26]. The electron temperature stays nearly constant within the visible e-beam plasma region of about 7.5 mm and drops by about 50% over a radial distance of 40 mm (figure 6(a)). Previous experiments and modeling showed a similar profile and magnitude of electron temperature [10, 14, 26]. This is consistent with the work of Petrova *et al*, who showed that in the presence of an

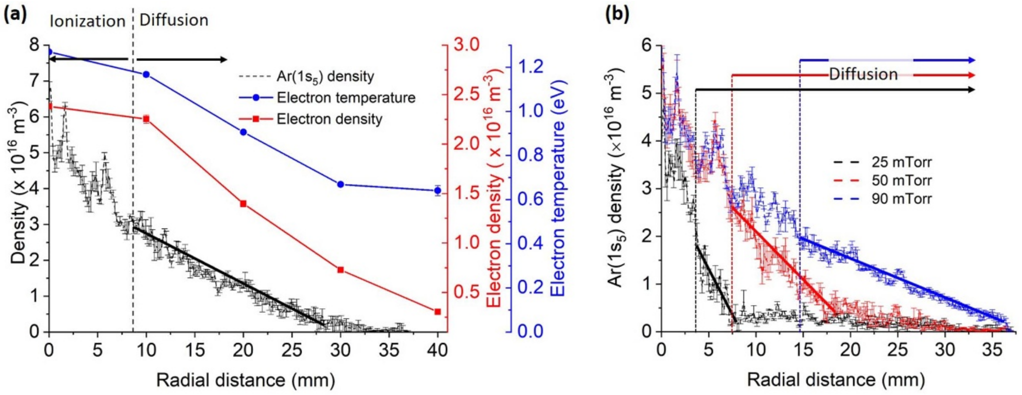

Figure 6. (a) Electron density, temperature and Ar($1s_5$) density as a function of distance at a pressure of 60 mTorr and (b) Radial profile of Ar($1s_5$) at pressures of 25, 50 and 90 mTorr. The region to the left of the color coded vertical lines is the ionization zone and the region to their right is the diffusive zone at their respective pressures.

acceleration grid at a pressure of 60 mTorr and a magnetic field of 200 G, the electron temperature remains constant over a radial distance of about 15 mm from the center of the discharge and drops by about 50% over a radial distance of 40 mm [26]. The absence of the acceleration grid in our e-beam plasma and a difference in the applied magnetic field likely results in our observed difference in the size of the constant electron temperature region. The Ar($1s_5$) radial density profile displays two distinct regions. There is an abrupt change in the radial Ar($1s_5$) density gradient for radii $r > \sim 7.5$ mm (figure 6(a)). These distinct transport regions in the Ar($1s_5$) density profile persists at different pressures (figure 6(b)). Evidently, the location of this boundary between the inner and outer transport region varies with pressure.

The Ar($1s_5$) density peaks in the center of the e-beam and decreases with radial distance from the center of the discharge (figure 6(b)). Petrova *et al* analyzed the radial profile of the plasma by dividing the spatial region into two zones: the ionization zone and the diffusive zone. The excitation by the e-beam and ionization occurs in the ionization zone, while species diffuse and recombine in the diffusive zone. The linear spatial density profile of Ar($1s_5$) observed outside the ionization region is indicative of steady-state diffusion governed by the Fick's law of diffusion ($\nabla^2 n_{\mathrm{Ar}(1s_5)} = 0$), which applies in the absence of local sources or sinks. This suggests that metastables are primarily generated in the electron beam region and subsequently diffuse outward without significant production or loss in the periphery. The ionization zone and the diffusive zones have been identified in figures 6(a) and (b) by identifying the linear slope of the Ar($1s_5$) density drop. The scattering of the intermediate energy electrons with energy > 11.5 eV, responsible for Ar($1s_5$) production increases with pressure due to enhanced collision rates. Hence, the size of the ionization zone depends on pressure [26] and it increases with pressure (figures 6(a) and (b)). The observation of the diffusive zone suggests that there is negligible production of Ar($1s_5$) outside the ionization zone. The Ar($1s_5$) diffuse and recombine in this region outside the ionization zone, without any additional production. The size of the ionization zone was found to be similar to the size of the visible plasma emission region. While the peak Ar($1s_5$) density at the center of the discharge saturates with pressure beyond 60 mTorr, the radial distance to which the Ar($1s_5$) reach increases with pressure.

4. Conclusion

The radial density profile of the Ar($1s_5$) metastable level was measured using laser-induced fluorescence in an e-beam confined in a magnetic field. We report the experimental validation of two transport regions of the Ar($1s_5$) metastables using laser-induced fluorescence, which confirms previous simulation work. Their density was found to increase with pressure at the center of the discharge and saturate with the increase in pressure. This saturation can be primarily attributed to a significant increase in electron-impact quenching rates, dominantly by the reaction $\mathrm{Ar}(1s_5) + e^- \rightarrow \mathrm{Ar}(1s_4) + e^-$, which becomes increasingly dominant at higher pressures. While the bulk electron density increases by approximately a factor of 7, the density of the Ar($1s_5$) metastable level, primarily generated by electrons with energies exceeding 11.54 eV, only increases by a factor of about 1.3 before reaching saturation. This limits the achievable metastable density despite an increase in the electron density. This disparity suggests that the high-energy tail of the EEDF responsible for metastable excitation, does not scale with pressure in the same manner as the lower-energy electron population (<6 eV). Future work focused on a detailed characterization of the EEDF in the energy range above 11.54 eV can provide insights into the production mechanisms of the Ar($1s_5$) metastable state and its pressure-dependent saturation behavior. The peak electron and Ar($1s_5$) densities were found to be of the order of 10^{16} m^{-3}, while the electron temperature was typically less than an eV. The ionization zone and the diffusion zone of the plasma were identified from the spatial profile of the Ar($1s_5$) level, with a clear linear gradient in the diffusion zone. This linearity confirms negligible production or loss in that region, reinforcing the concept that metastables are generated centrally and transported outward. This spatial demarcation coincides with the visible plasma emission profile. Argon metastables, with their substantial internal energy, can efficiently transfer energy beyond their production zone, making them highly valuable for material processing applications.

Data availability statement

All data that support the findings of this study are included within the article (and any supplementary files).

Acknowledgments

This work was supported by US Department of Energy, office of Fusion Energy Sciences through contract DE-AC02-09CH11466.

ORCID iDs

V S Santosh K Kondeti 0000-0001-8825-845X
Nirbhav S Chopra 0000-0003-4407-7395
Shurik Yatom 0000-0001-8716-8487
Yevgeny Raitses 0000-0002-9382-9963

References

[1] Adamovich I *et al* 2022 *J. Phys. D: Appl. Phys.* **55** 373001
[2] Parsons G N and Clark R D 2020 *Chem. Mater.* **32** 4920–53
[3] Knoops H C, Faraz T, Arts K and Kessels W M 2019 *J. Vac. Sci. Technol. A* **37** 030902
[4] Oehrlein G, Metzler D and Li C 2015 *ECS J. Solid State Sci. Technol.* **4** N5041
[5] Dorf L, Wang J C, Rauf S, Zhang Y, Agarwal A, Kenney J, Ramaswamy K and Collins K 2016 Atomic precision etch using a low-electron temperature plasma *Proc. SPIE* **9782** 30–37
[6] Stefanović I, Kuschel T, Schröter S and Böke M 2014 *J. Appl. Phys.* **116** 113302
[7] Sukhinin G, Fedoseev A and Khmel' S Y 2008 *Plasma Phys. Rep.* **34** 60–70
[8] Sansonnens L, Howling A, Hollenstein C, Dorier J L and Kroll U 1994 *J. Phys. D: Appl. Phys.* **27** 1406
[9] Walton S, Boris D, Hernández S, Lock E, Petrova T B, Petrov G and Fernsler R 2015 *ECS J. Solid State Sci. Technol.* **4** N5033
[10] Lock E, Fernsler R and Walton S 2008 *Plasma Sources Sci. Technol.* **17** 025009
[11] Lock E H, Petrovykh D Y, Mack P, Carney T, White R G, Walton S G and Fernsler R F 2010 *Langmuir* **26** 8857–68
[12] Lock E H, Walton S G and Fernsler R F 2009 *Plasma Process. Polym.* **6** 234–45
[13] Yatom S, Chopra N, Kondeti S, Petrova T B, Raitses Y, Boris D R, Johnson M J and Walton S G 2023 *Plasma Sources Sci. Technol.* **32** 115005
[14] Rauf S, Balakrishna A, Agarwal A, Dorf L, Collins K, Boris D R and Walton S G 2017 *Plasma Sources Sci. Technol.* **26** 065006
[15] Lock E, Petrova T B, Petrov G, Boris D and Walton S 2016 *Phys. Plasmas* **23** 043518
[16] Petrov G, Boris D, Petrova T B, Lock E, Fernsler R and Walton S 2013 *Plasma Sources Sci. Technol.* **22** 065005
[17] Boris D, Petrov G, Lock E, Petrova T B, Fernsler R and Walton S 2013 *Plasma Sources Sci. Technol.* **22** 065004
[18] Leonhardt D, Muratore C, Walton S G and Meger R A 2004 *Surf. Coat. Technol.* **188** 299–306
[19] Walton S, Hernández S, Boris D, Petrova T B and Petrov G 2017 *J. Phys. D: Appl. Phys.* **50** 354001
[20] Kondeti V S S K, Yatom S, Romadanov I, Raitses Y, Dorf L and Khomenko A 2024 *J. Vac. Sci. Technol. A* **42** 063005
[21] Godyak V and Demidov V 2011 *J. Phys. D: Appl. Phys.* **44** 233001
[22] Lieberman M A and Lichtenberg A J 2005 *Principles of Plasma Discharges and Materials Processing* (Wiley) (https://doi.org/10.1002/0471724254)
[23] Druyvesteyn M J 1930 *Z. für Phys.* **64** 781–98
[24] Hobbs G D and Wesson J A 1967 Heat flow through a Langmuir sheath in the presence of electron emission Plasma Phys. **9** 85–7
[25] Demidov V I, Ratynskaia S V and Rypdal K 2002 Electric probes for plasmas: The link between theory and instrument *Review of Scientific Instruments* **73** 3409–39
[26] Petrova T B, Boris D, Petrov G, Johnson M and Walton S 2024 *Phys. Plasmas* **31** 043515
[27] Petrov G, Giuliani J and Dasgupta A 2002 *J. Appl. Phys.* **91** 2662–77
[28] Wiese W, Brault J, Danzmann K, Helbig V and Kock M 1989 *Phys. Rev. A* **39** 2461
[29] Kramida A, Yu R and Reader J NIS ASD Team 2024 NIST Atomic Spectra Database (ver. 5.12) (National Institute of Standards and Technology) (available at: https://physics.nist.gov/asd) (Accessed 19 August 2025)
[30] Cheng Z-W, Zhu X-M, Liu F-X and Pu Y-K 2014 *J. Phys. D: Appl. Phys.* **47** 495205
[31] Zatsarinny O, Wang Y and Bartschat K 2014 *Phys. Rev. A* **89** 022706
[32] Scheller G R, Gottscho R A, Graves D and Intrator T 1988 *J. Appl. Phys.* **64** 598–606
[33] Carbone E, Graef W, Hagelaar G, Boer D, Hopkins M M, Stephens J C, Yee B T, Pancheshnyi S, Van Dijk J and Pitchford L 2021 *Atoms* **9** 16
[34] Pitchford L C *et al* 2017 *Plasma Process. Polym.* **14** 1600098
[35] Pancheshnyi S, Biagi S, Bordage M C, Hagelaar G, Morgan W, Phelps A and Pitchford L C 2012 *Chem. Phys.* **398** 148–53
[36] Chopra N S, Romadanov I and Raitses Y 2024 *Plasma Sources Sci. Technol.* **33** 125003